SUPPORTING INFORMATION

Engineering Three-Dimensional Hybrid Supercapacitors and Micro-Supercapacitors for High-Performance Integrated Energy Storage

Maher F. El-Kady[a,b], Melanie Ihns[a], Mengping Li[a], Jee Youn Hwang[a], Mir F. Mousavi [a,c], Lindsay Chaney[a], Andrew T. Lech[a] and Richard B. Kaner[a,d,1]

[a]Department of Chemistry and Biochemistry and California NanoSystems Institute, University of California, Los Angeles (UCLA), Los Angeles, California 90095, USA.

[b]Department of Chemistry, Faculty of Science, Cairo University, Giza 12613, Egypt.

[c]Department of Chemistry, Tarbiat Modares University, Tehran 14115-175, Iran.

[d]Department of Materials Science and Engineering, UCLA, Los Angeles, California 90095.

[1]To whom correspondence should be addressed. E-mail: kaner@chem.ucla.edu

Keywords: supercapacitor | micro-supercapacitor | graphene | metal oxide

1. Rational design of high-performance hybrid supercapacitors. To achieve high-energy and high-power supercapacitors, one needs to facilitate both the ionic and electronic currents within the electrodes. This is very challenging especially with metal oxide pseudo-capacitors because of the low electrical conductivity and long ionic diffusion pathways of conventional metal oxide films. Thus, in conventional compact MnO_2 thick film electrodes, only the top layer is exposed to the electrolyte, meaning that a limited amount of the active material is involved in charge storage, Fig. 1A. To solve these problems, various approaches have been explored in the literature. For example, the electrochemical utilization of electrodes was improved by using nanostructured MnO_2 such as nanoparticles, nanorods, nanowires and nanoflowers [1-2]. The porous structure of these electrodes maximizes the area of active material that is exposed to the electrolyte and thus available to discharge compared to a solid electrode surface, Fig. 1B. Although this system exhibits higher energy density, it still suffers from the inherently low electrical conductivity of MnO_2 leading to low power output. To improve the electrical conductivity of MnO_2 film, conductive materials such as carbon powder, carbon nanotubes and graphene have been introduced into nanostructured MnO_2 electrodes [3]. However, the electronic charge carriers must move through small inter-particle contact areas which exhibit additional resistance resulting in poor electron transport from the electrode material to the current collector, Fig. 1C. An ideal electrode would be obtained by growing MnO_2 nanostructures onto a 3D interconnected macro-porous graphene framework with high electrical conductivity and high surface area, Fig. 1D. In this structure, the conducting graphene framework acts as a 3D current collector to provide electron “superhighways” for charge storage and delivery, while the nanostructured MnO_2 enables fast, reversible Faradaic reactions with short ionic diffusion pathways. Another interesting feature of this structure is that each MnO_2 nanoparticle is electrically connected to the current collector so that all the nanoparticles contribute to capacity with almost no “dead” mass.

2. Graphene/metal oxide nanocomposites: The microstructure of the host graphene matters!

Does the pore structure of the graphene electrode affect the electrochemical performance of its composites with metal oxides? To answer this question, we employed two forms of graphene of different pore structures in this study: chemically converted graphene (CCG) films and laser scribed graphene (LSG) films. The CCG sheets are well connected together in a layered structure to form the CCG electrodes. The reduced porosity and limited accessibility to electrolyte ions causes a slow frequency response of ~5 seconds for CCG electrodes (Figure S1). LSG electrodes, on the other hand, have a well-defined porous structure such that the individual graphene sheets in the LSG network are accessible to the electrolyte, and thus exhibit a rapid frequency response of 23 ms (Figure S2). This causes the enhanced capacitance and rate capability observed with the LSG/MnO_2. The optimized structure of LSG electrodes synergizes the effects of both effective ion migration and high electroactive surface area, thus enabling high and reversible capacitive behavior for LSG/MnO_2 even at high charge/discharge rates.

Further understanding of the capacitive behavior of the CCG/MnO_2 and LSG/MnO_2 hybrid electrodes was obtained by conducting ac impedance measurements in the frequency range 1 MHz to 10 mHz. For each of these cells, MnO_2 was electrodeposited for 120 min. The Nyquist plots consist of a spike at the low frequency region and a semicircle at the high frequency region (Figure S2). Compared with CCG/MnO_2, the LSG/MnO_2 supercapacitor shows a much smaller diameter for the semicircle, which suggests a more efficient charge transfer on the electrode surface. Furthermore, in the low frequency region, a more vertical straight line is observed for the porous LSG/MnO_2 electrodes, indicating faster ion diffusion and almost ideal capacitive behavior for these electrodes. The intercept of the Nyquist curve on the real axis is about 1.5 Ω, indicating a high conductivity for the electrolyte and low internal resistance of the electrodes (Figure S2). These results show the strong impact of the microstructure of the graphene electrodes on the electrochemical performance of their composites with metal oxides.

The LSG/MnO_2 has just the right porosity that provides good accessibility to the electrolyte during charge and discharge processes, while at the same time still maintains the high packing density of the material. Furthermore, the high surface area of nanostructured MnO_2 provides more active sites for the Faradaic reactions and shortens the ion diffusion pathways that are crucial for realizing its full pseudo-capacitance. This explains why the LSG/MnO_2 electrodes achieve both high gravimetric capacitance and volumetric capacitance superior to those previously reported for MnO_2 based pseudo-capacitors and hybrid capacitors, see table S1.

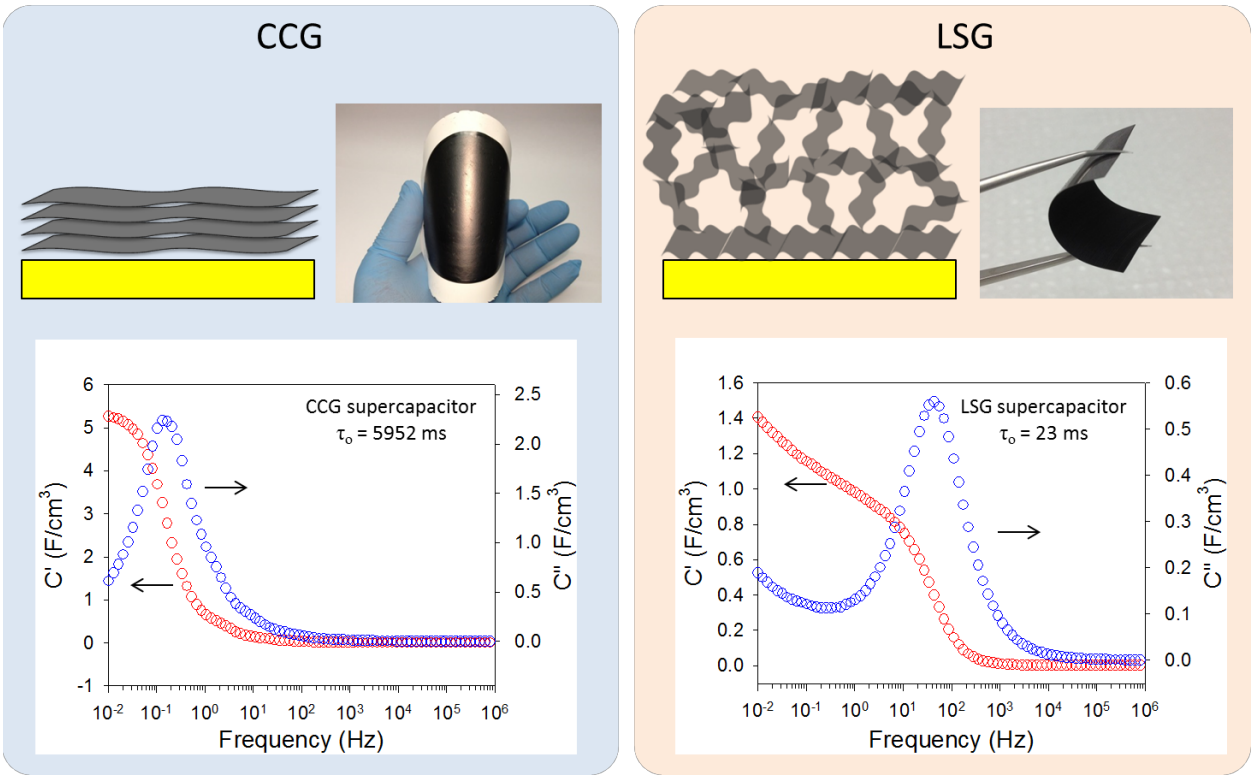

Figure S1: Effect of the pore structure of graphene on its electrochemical performance. Top: Schematic illustration showing the structural differences between dense CCG films and porous LSG films. Bottom: The emergence of real (C') and imaginary (C'') parts of the volumetric stack capacitance versus frequency for CCG and LSG electrodes.

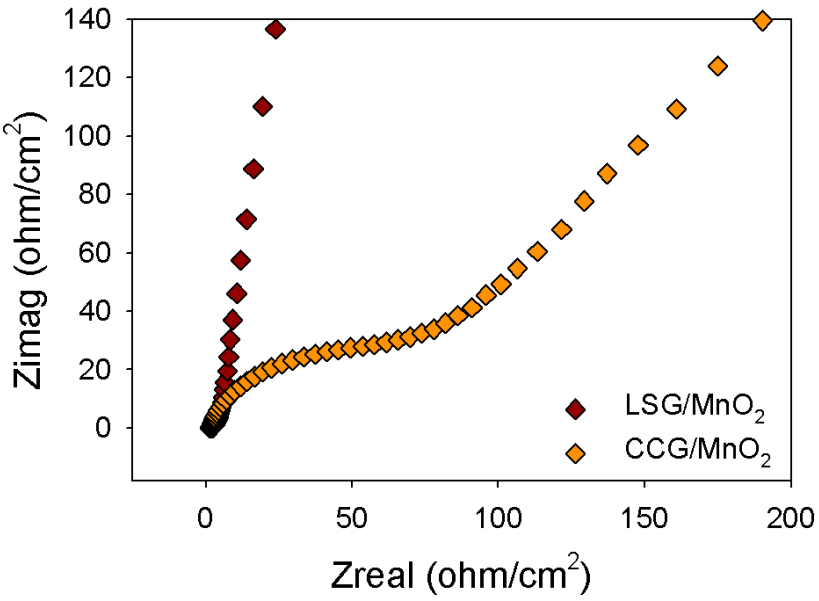

Figure S2: Nyquist impedance plots of CCG/MnO_2 and LSG/MnO_2. The LSG/MnO_2 shows better ion diffusion and smaller charge transfer resistance. The experiments were carried out over a frequency range of 1 MHz to 10 mHz.

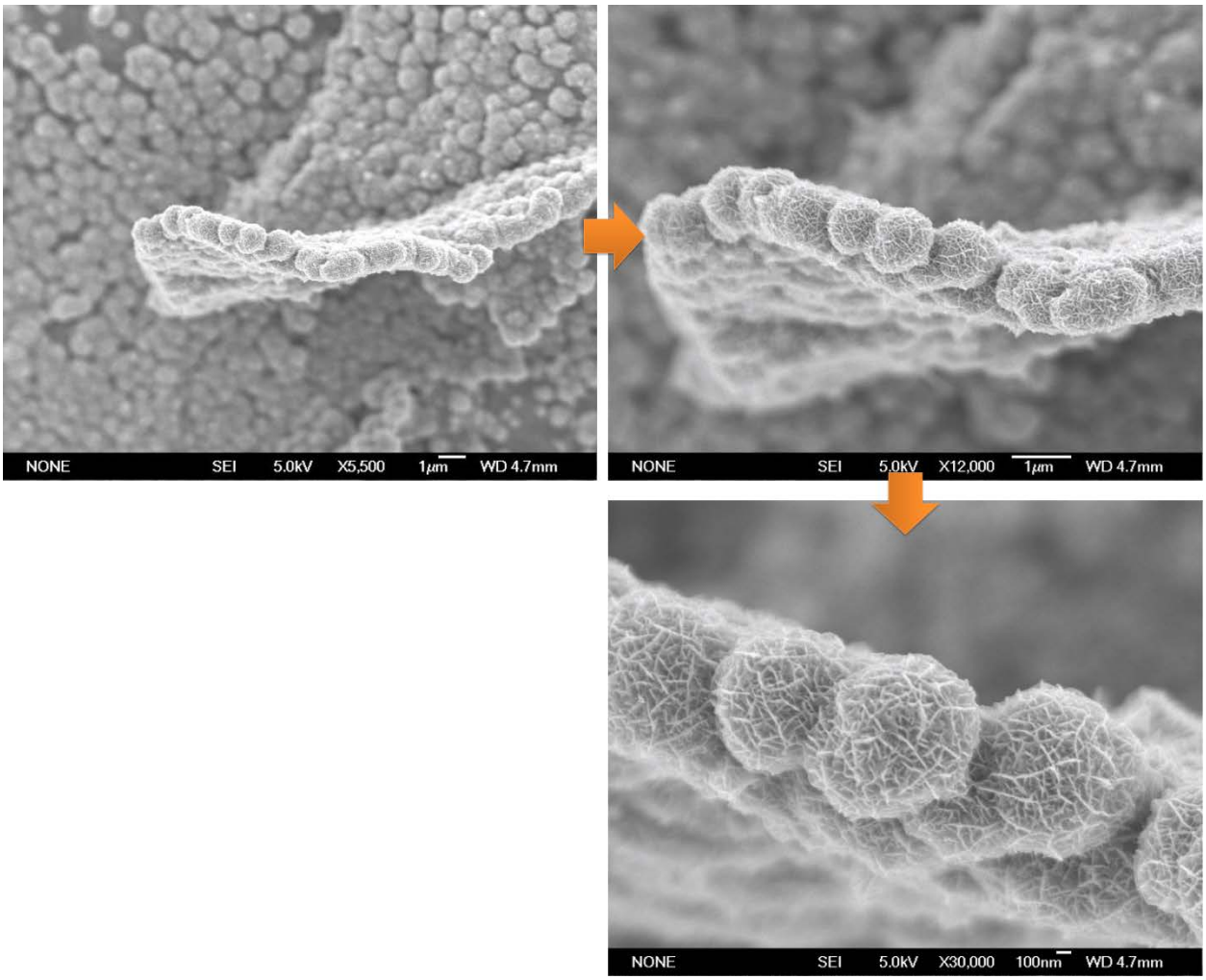

Figure S3: Evolution of the surface of LSG/MnO_2. SEM analysis of the surface of LSG/MnO_2 electrodes shows a homogeneous coating of the surface of graphene with MnO_2 nanoflowers.

3. Asymmetric Supercapacitors: Asymmetric supercapacitors make use of positive and negative electrode materials of different types that can be charged/discharged in well-separated potential windows in the same electrolyte. They have attracted attention because they offer high capacity via a Faradaic reaction at the positive electrode and maintain fast charge/discharge due to the EDL mechanism at the negative electrode. Moreover, the asymmetric configuration can extend the operating voltage window of aqueous electrolytes beyond the thermodynamic limit of water (about 1.2 V), leading to significantly higher specific energy than symmetric supercapacitors using aqueous electrolytes. In fact, asymmetric supercapacitors based on carbon and NiOOH electrodes with an aqueous electrolyte are now commercially available from ESMA-ELTON (4). However, while this configuration ensures high capacitance, it has a low cell voltage (<1.5 V) that is detrimental to its energy and power performance.

4. Direct fabrication of hybrid micro-supercapacitor array for high voltage applications.

Supercapacitors are widely used in a variety of applications where a large amount of power is needed for a short period of time, where a very large number of charge/discharge cycles or a longer lifetime is required. However, the working voltage of existing supercapacitors is very low (<3 volts), whereas traditional capacitors used for general electronics applications typically range from a few volts to 1 kV. To meet the high voltage requirements, supercapacitors are often put into a bank of cells connected together in series (5). This results in bulky supercapacitor modules which are appropriate in some cases, but often cause problems in applications where the total size of the power source is critical. Here, we propose a different design in which an array of separate electrochemical cells are directly fabricated in the same plane as shown in Figures S4-S8.

First, circuits are designed using appropriate computer software and are directly patterned on a graphite oxide film coated on a DVD disc. Figure S4 shows a DVD after the direct writing of LSG patterns designed to achieve symmetric and asymmetric micro-supercapacitor arrays. It is also

possible to design patterns to make a supercapacitor bank of series/parallel combinations in order to meet the voltage (series) and current (parallel) requirements of the system on which they will be integrated.

The second step is the deposition of MnO_2 nanoflowers. Here, the deposition process varies depending on whether it is a symmetric or an asymmetric array. For an asymmetric array, the process is explained in Figures S5-S6 and for a symmetric array in Figure S7. A full set of symmetric and asymmetric supercapacitor arrays are shown in Figure S8 and their electrochemical performance in Figure S9. Ideally a gel electrolyte is used to prevent leakage into other cells in the array.

These arrays offer the flexibility of controlling the output voltage and current of the array. For example, compared with a single device with an operating voltage of 2 V, an array of 3 serial cells extends the output voltage to 6 V, whereas the output capacity (runtime) can be increased by a factor of 3 using an array of 3 cells connected in parallel (Fig. S9). By using an array of 3 strings in parallel and 3 strings in series, the output voltage and current can both be tripled. Although we demonstrated the high-voltage supercapacitor array using a string of 3 cells, it is possible to increase the number of cells to reach an operating voltage of 100 V, which would be promising for a variety of applications.

5. Integration of Micro-supercapacitor array with solar cells for simultaneous solar energy harvesting and storage.

With growing interest in "green" systems, solar power is gaining popularity for the implementation in more energy efficient buildings and smart cities. When combined with an energy storage system for storing energy during the day, they can be used to make self-powered systems that are promising for streetlight, industrial wireless monitoring, transportation and consumer

electronics applications (6). Chemical batteries are often used in these systems due to their high energy density. Recently, supercapacitors are emerging as alternatives because they can capture energy more efficiently due to their short response time. These modules are struggling, though, because of the low energy density of existing supercapacitors. Since LSG/MnO_2 hybrid supercapacitors can provide higher energy density and because they can be fabricated in arrays with high voltage and current ratings, they can be integrated with solar cells for highly efficient energy harvesting and storage (Fig. 8b).

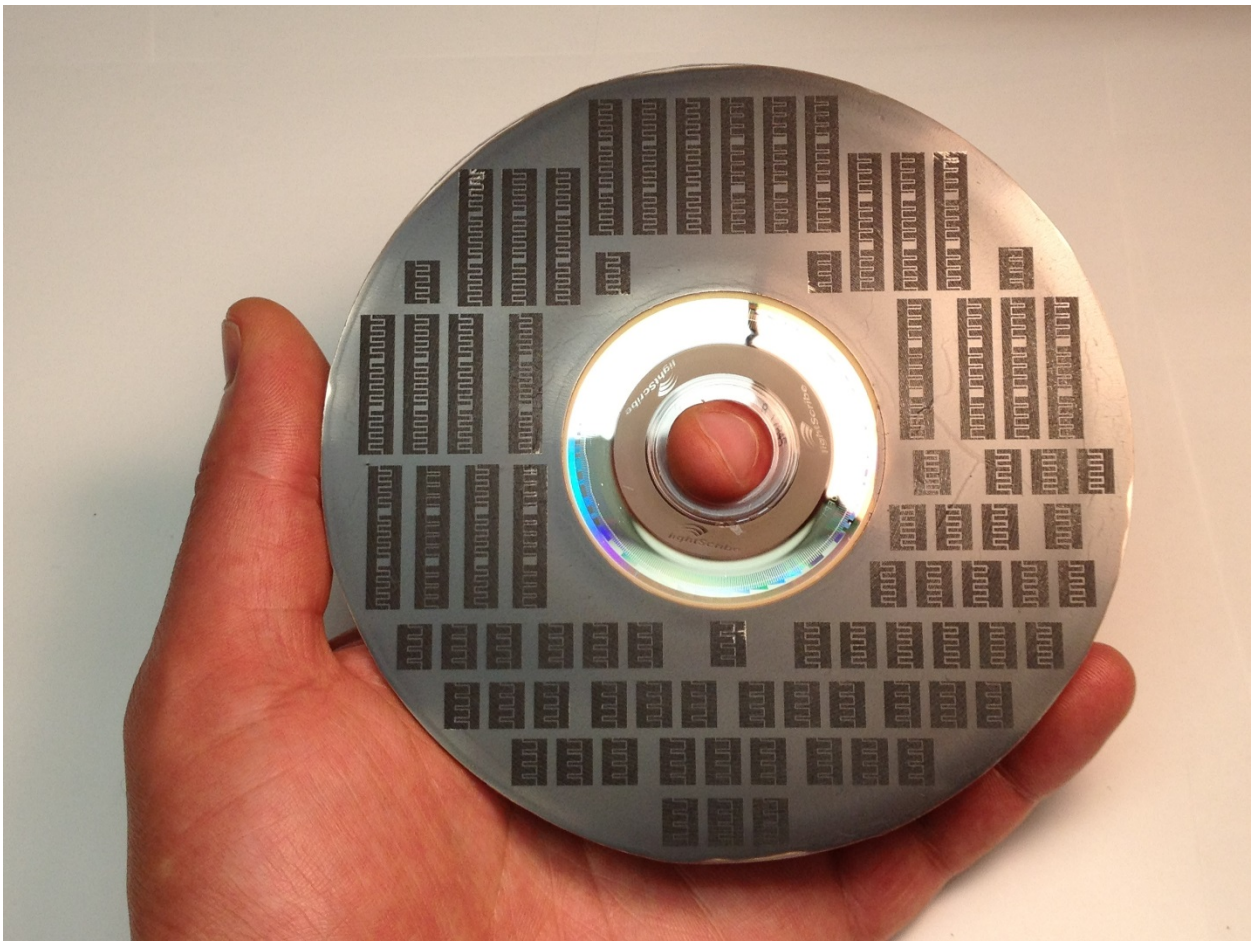

Figure S4: LightScribe writing of LSG micro-supercapacitor arrays: The pattern is designed with Microsoft Paint software and then directly patterned on a GO coated DVD disc. The device consists of 8 in-plane microelectrodes (4 positive and 4 negative) separated by nearly insulating GO and the distance between the microelectrodes is close enough to keep the ion-transport pathway short.

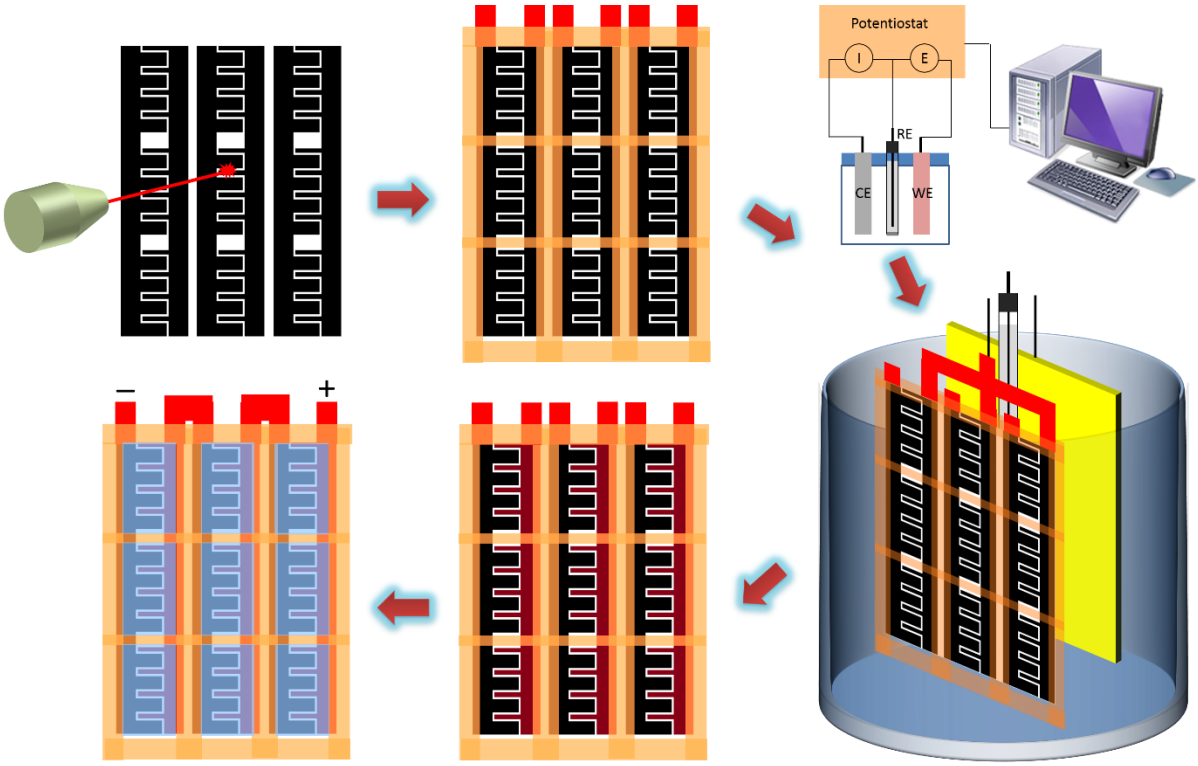

Figure S5: Fabrication of an array of 9 asymmetric cells connected in series/parallel: The plain graphene array is first made as explained in Figure S4. In this example, the graphene pattern is designed to make an array of 9 cells (3 in parallel X 3 in series). This is followed by the electro-deposition of MnO_2 in a three electrode cell as schematically illustrated in the figure. Since this is an asymmetric supercapacitor, the deposition is controlled to go on three sets of micro-electrodes (the positive electrodes) and the other three are kept intact (negative electrodes). It is worth mentioning that the MnO_2 deposition occurs on the 9 cells at the same time. This means that the fabrication of the supercapacitor array takes almost the same time as a single cell without the need for further processing. After the deposition is complete, the supercapacitor array is thoroughly washed with DI water and the electrolyte is added onto each of the cells. The full micro-supercapacitor array is shown in Figure S6.

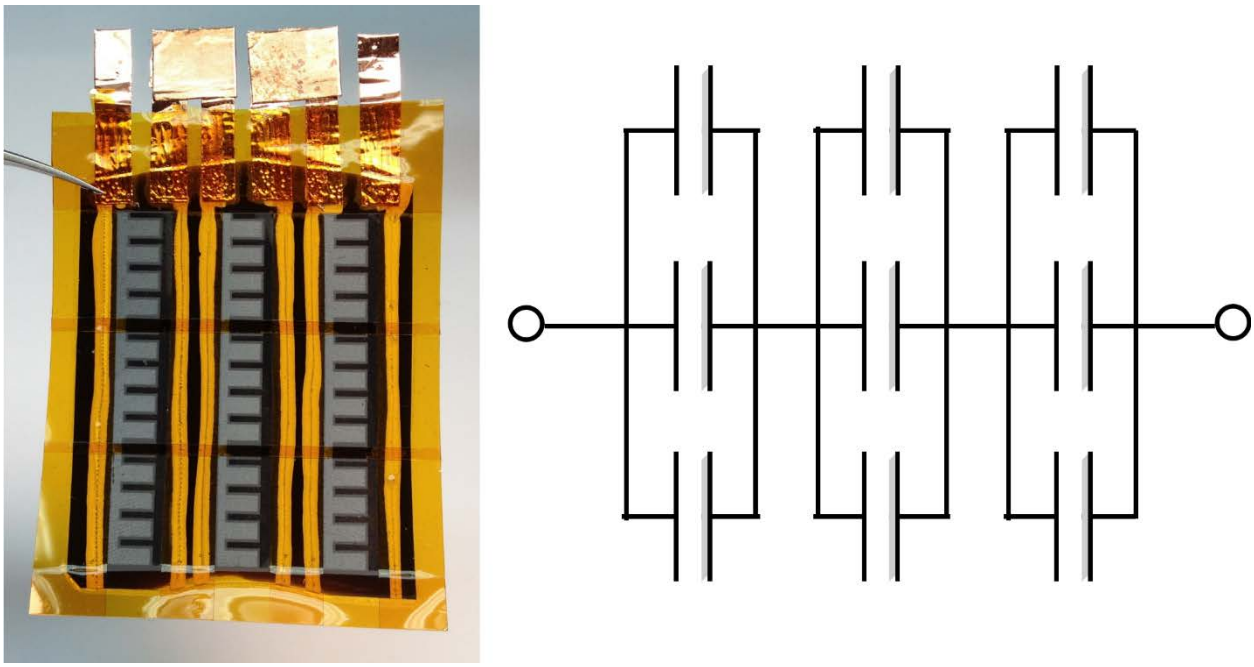

Figure S6: The finished array of 9 asymmetric cells connected 3 in series X 3 in parallel.

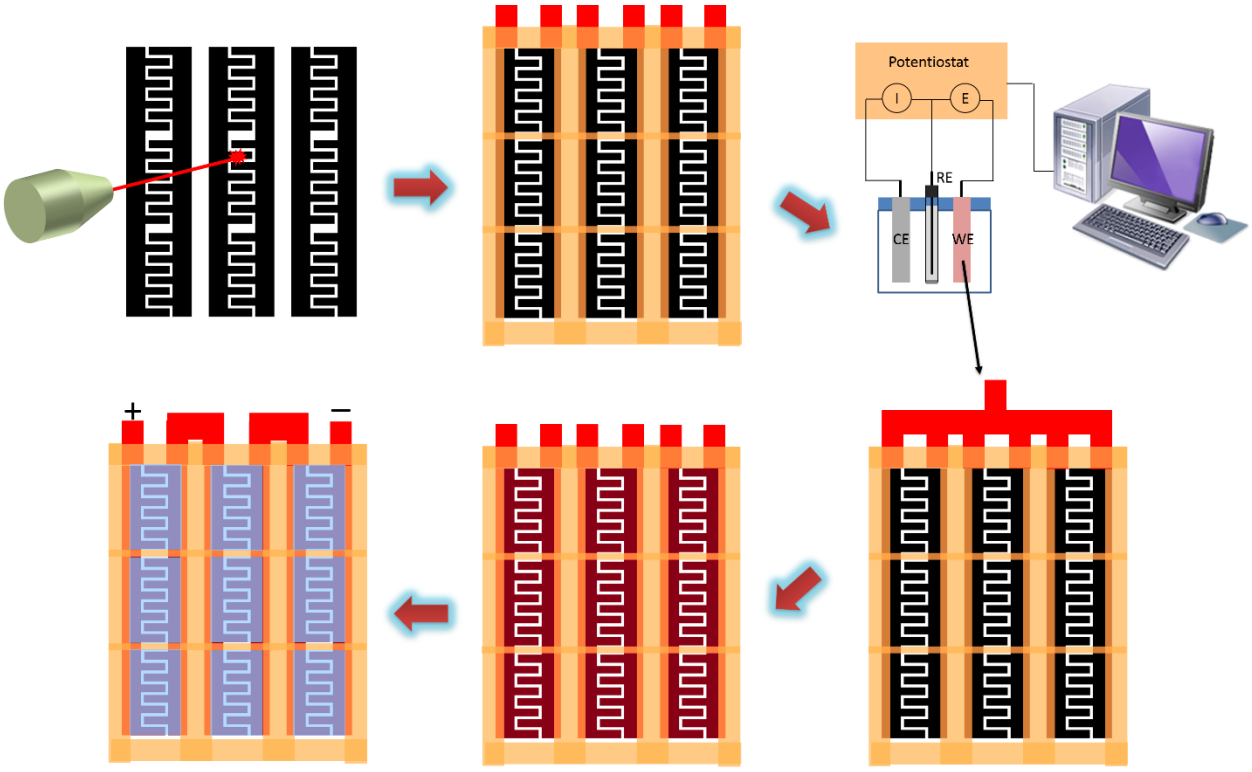

Figure S7: Fabrication of an array of 9 symmetric supercapacitors connected in series/parallel. The fabrication method is similar to that explained in Figure S5 except that all six sets of micro-supercapacitor electrodes act as the working electrode during the deposition of MnO_2 instead of the three shown in Figure S5.

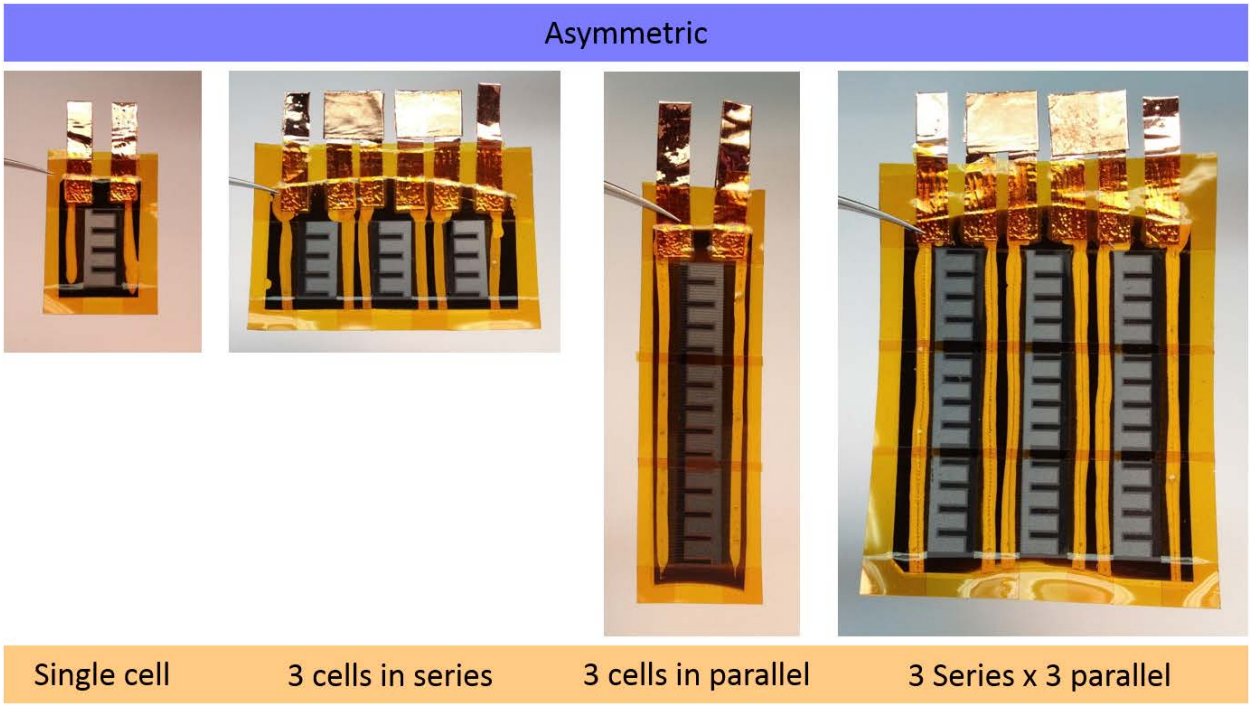

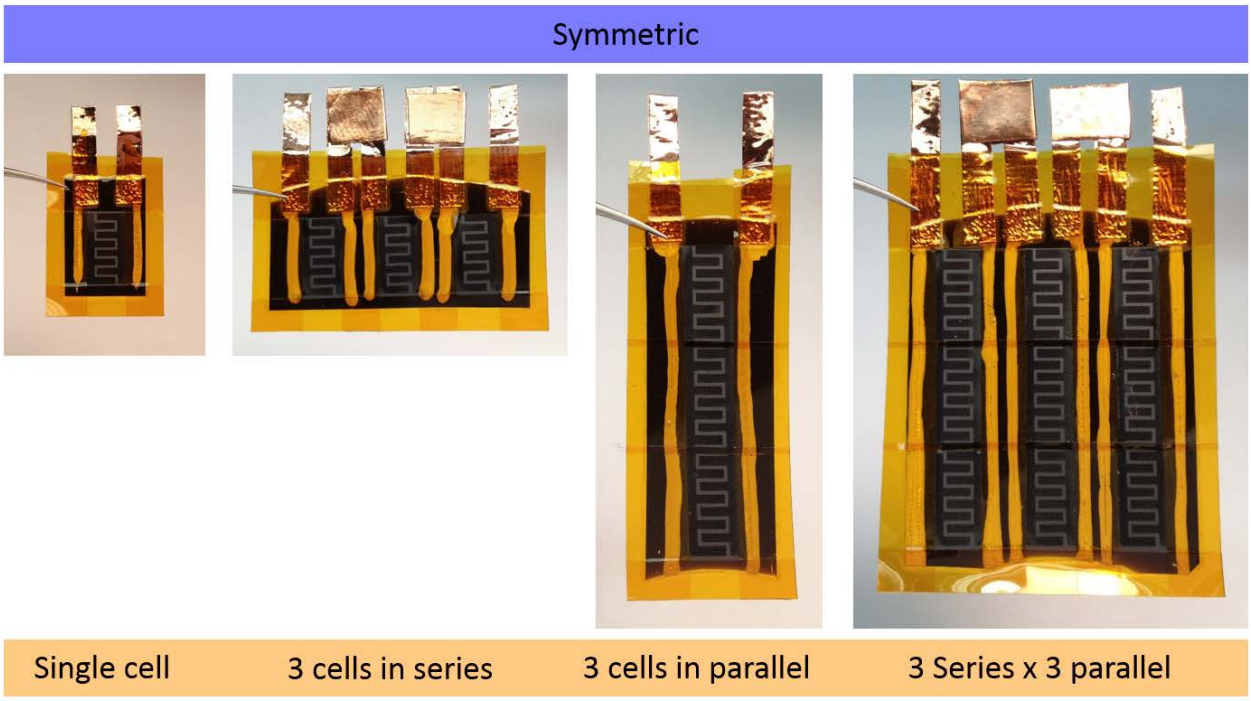

Figure S8: Demonstration of supercapacitor arrays that are connected in series, parallel and in combinations of the two. This can be done for both symmetric and asymmetric cells.

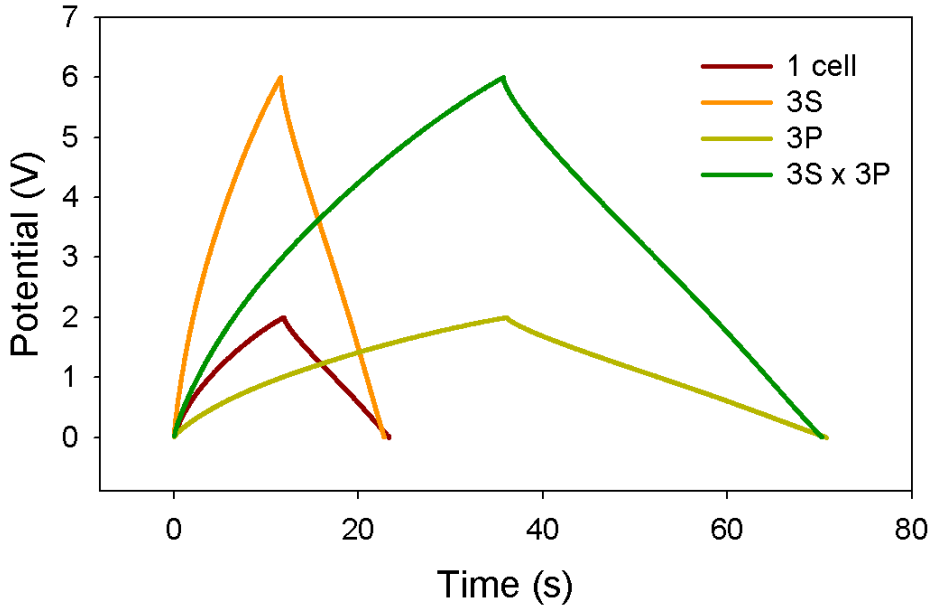

Figure S9: The electrochemical performance of asymmetric supercapacitor arrays. Galvanostatic charge/discharge curves of asymmetric supercapacitor arrays connected in series (3S), in parallel (3P), and in a combination of series and parallel (3S x 3P). A single device is shown for comparison. Compared with the single device with an operating voltage of 2 V, the serial connection extends the output voltage to 6 V, whereas the output capacity (runtime) can be increase by a factor of 3 using the parallel connection. By using a combination of series/parallel connections, the output voltage and current can both be tripled.

Electrode Material	Cell Type	Voltage window	Electrolyte	Specific capacitance		Ref.
				Per Footprint area (mF/cm^2)	Volumetric (F/cm^3)	
Activated carbons	Full cell	2.7 V	$TEABF_4$/AN	~300	60-80	7
Carbide derived carbon	3 electrode	2.3 V	$TEABF_4$/AN	–	180	8
LSG	Full cell	4.0 V	$EMIMBF_4$	5.02	14.34	9
Activated MEGO	Full cell	3.5 V	BMIM-BF_4/AN	–	60	10
Liquid mediated CCG	Full cell	3.5 V	$EMIMBF_4$/AN	–	263.3	11
CNT/PPy/MnO_2	Full cell	0.9 V	KCl	–	16.1	12
Graphene/MnO_2/CNT	Full cell	1.0 V	1.0 M Na_2SO_4	–	130	13
CNT/MnO_2	3 electrode	0.85 V	0.1 M K_2SO_4	–	246	14
Meso-porous carbon/MnO_2	3 electrode	0.8 V	1.0 M Na_2SO_4	–	108	15
Ultra-porous Carbon/MnO_2	3 electrode	0.8 V	1.0 M Na_2SO_4	1500*	90	16
Graphene/RuO_2	3 electrode	1.0 V	1.0 M H_2SO_4	–	(570 F/g)#	17
CNT/Co_3O_4	3 electrode	0.5 V	2.0 M KOH	30.8	30.8	18
Titanium carbide clay	3 electrode	0.55 V	1.0 M H_2SO_4	–	910 @5 µm 534 @30 µm 355 @75 µm	19
MXene/PVA	3 electrode	0.6 V	1.0 M KOH	–	528	20
LSG/MnO_2 (15 µm thick film)	Full cell	0.9 V	1.0 M Na_2SO_4	852	1136.5	This work

Table S1: Electrochemical performance of supercapacitors featuring a variety of electrodes materials such as carbons, polymers, MnO_2 and their hybrid materials. AN: Acetonitrile; $TEABF_4$: tetraethylammonium tetrafluoroborate; $EMIMBF_4$: 1-ethyl-3-methylimidazolium tetrafluoroborate; $BMIMBF_4$: 1-butyl-3-methyl-imidazolium tetrafluoroborat. # Since the volumetric capacitance is not reported, we use the gravimetric capacitance instead. *notice that the capacitance per footprint area in 3 electrode measurements is at least two times the areal capacitance for 2 electrode measurements (21).

Electrode Material	Cell Type	Voltage window	Electrolyte	Specific capacitance		Ref.
				Per Footprint area (mF/cm^2)	Volumetric (F/cm^3)	
Carbon onions	Full cell	3.0 V	$TEABF_4$/PC	1.7	1.35	22
Graphene	Full cell	1.0 V	PVA-H_2SO_4	2.32	3.05	23
Graphene	Full cell	2.5 V	Ionogel*	1.78	2.35	23
Graphene-CNT carpet	Full cell	1.0 V	1.0 M Na_2SO_4	2.16	1.08	24
Graphene/CNT	Full cell	1.0 V	3.0 M KCl	5.1	3.1	25
Carbide-derived carbon	Full cell	2.3 V	$TEABF_4$/AN	–	180	8
Polyaniline nanowires	Full cell	1.0 V	1.0 M H_2SO_4	–	588	26
Activated cabon-MnO_2	Full cell	1.0-1.5 V	0.2 M K_2SO_4	21.3-30	–	27
MnO_2	Full cell	1.0 V	0.2 M K_2SO_4	28.3	–	27
VS_2 nanosheets	Full cell	0.6 V	PVA–$BMIMBF_4$	4.76	317	28
MoS_2 nanosheets	Full cell	0.5 V	–	8	178	29
LSG/MnO_2	Full cell	0.9 V	1.0 M Na_2SO_4	384	1136.5	This work

Table S2: Electrochemical performance of interdigitated micro-supercapacitors. *Ionogel: 1-butyl-3-methylimidazolium bis(trifluoromethylsulfonyl)imide ionic liquid gelled with fumed silica nanopowder.

SI Materials and Methods

After electro-deposition, the working electrode was thoroughly washed with DI water to remove the excess electrolyte and dried in an oven at 60 °C for 1 h. The amount of MnO_2 deposited on the LSG framework was determined from the difference in weight of the electrode before and after electro-deposition using a high precision microbalance with a readability of 1 μg (Mettler Toledo, MX5).

For comparison, MnO_2 was electrodeposited on other substrates such as gold-coated polyimide and graphene (CCG) paper. The gold-coated polyimide was obtained from Astral Technology Unlimited, Inc. (Minnesota, USA) and used without further treatment. The graphene paper was produced following our previously reported method (30). The gold-coated polyimide and graphene paper were cut into rectangular strips of 1 cm^2 for further electro-deposition of MnO_2 under the same conditions as described above.

Assembly of sandwich-type hybrid supercapacitors. Hybrid supercapacitors with the conventional sandwich structure were assembled using electrodes prepared in the previous section. Both symmetric and asymmetric supercapacitors were constructed. Symmetric supercapacitors were assembled by sandwiching a Celgard M824 (Celgard, North Carolina, USA) separator between two identical electrodes using 1.0 M Na_2SO_4 aqueous solution as the electrolyte. In the asymmetric structure, LSG/MnO_2 was used as the positive electrode and LSG as the negative electrode. For the LSG- and CCG-based supercapacitors, stainless steel (or copper) tape was attached to the electrodes, using silver paint, as the current collector. Before assembly, the electrodes were soaked in the electrolyte for 1 h to ensure proper wetting.

Fabrication of interdigitated hybrid micro-supercapacitors. The fabrication process of a micro-supercapacitor is illustrated in Figure 6 and described below. First, LSG interdigitated

microelectrodes were printed directly on a GO film supported on a gold coated polyimide (or a polyethylene terephthalate) substrate using a consumer grade DVD burner (23). Second, MnO_2 nanoflowers were grown on one set of the interdigitated electrodes using the electro-deposition setup described above. The applied current was normalized to the active LSG deposition area at a current density of 250 $\mu A/cm^2$ and the mass loading was controlled by adjusting the deposition time. Likewise, symmetric micro-supercapacitors based on LSG/MnO_2 as both the positive and the negative electrodes were prepared as well. Here, the fabrication process is the same except that the two sides (instead of one side) of the bare interdigitated LSG electrodes were connected together using copper tape and used as the working electrode during electro-deposition.

Characterization and measurements. The morphology and microstructure of the different electrodes were investigated by means of field emission scanning electron microscopy (JEOL 6700) equipped with energy dispersive spectroscopy (EDS) and optical microscopy (Zeiss Axiotech 100). XPS analysis was performed using a Kratos Axis Ultra DLD spectrometer. The thicknesses of the different components of the device were measured using cross-sectional scanning electron microscopy and a Dektak 6 profilometer. The electrochemical performances of the LSG-MSC supercapacitors were investigated by cyclic voltammetry (CV), galvanostatic charge/discharge tests and electrochemical impedance spectroscopy (EIS). CV testing was performed on a VersaSTAT3 electrochemical workstation (Princeton Applied Research, USA). Charge/discharge and EIS measurements were recorded on a VMP3 workstation (Bio-Logic Inc., Knoxville, TN) equipped with a 10 A current booster. EIS experiments were carried out over a frequency range of 1 MHz to 10 mHz with an amplitude of 10 mV at open-circuit potential. Calculations of the specific capacitance and the energy and power densities are discussed in detail in the following sections.

Calculations. The capacitances of the supercapacitors were calculated based on both cyclic voltammetry (CV) profiles and galvanostatic charge/discharge curves (CC). For the CV technique, the capacitance was calculated by integrating the discharge current (i) vs. potential (E) plots using the following equation:

$$C_{device} = \frac{\int idV}{v \times \Delta E} \qquad (1)$$

where v is the scan rate (V/s) and ΔE is the operating potential window.

The capacitance was also calculated from the charge/discharge (CC) curves at different current densities using the formula:

$$C_{device} = \frac{i_{app}}{dE/dt} \qquad (2)$$

where i_{app} is the current applied (in amps, A), and dV/dt is the slope of the discharge curve (in volts per second, V/s). Specific capacitances were calculated based on the area and the volume of the device stack according to the following equations:

$$Areal\ capacitance\ (C_A) = \frac{C_{device}}{A} \qquad (3)$$

$$Volumetric\ stack\ capacitance\ (C_v) = \frac{C_{device}}{V} \qquad (4)$$

where A and V refer to the area (cm^2) and the volume (cm^3) of the device, respectively. The stack capacitances (F/cm^3) were calculated taking into account the volume of the device stack. This includes the active material, the current collector and the separator with electrolyte.

The energy density of each device was obtained from the formula given in Equation (5):

$$E = \frac{1000}{2 \times 3600} C_v \Delta E^2 \qquad (5)$$

where E is the energy density in Wh/l, C_v is the volumetric stack capacitance obtained from galvanostatic charge/discharge curves using Equation (3) in F/cm^3 and ΔE is the operating voltage window in volts.

The power density of each device was calculated using the equation:

$$P = \frac{E}{t} \qquad (6)$$

where P is the power density in W/l and t is the discharge time in hours.

Since the majority of volumetric capacitances reported in the literature are based on the volume of the active material only, we did the same calculations for the purpose of comparison using the following equations:

Volumetric capacitance of the device,

$$C_{v(device)} = \frac{C_{device}}{V} \qquad (7)$$

where V is the volume of the active material on both electrodes

Volumetric capacitance per electrode,

$$C_{v(electrode)} = 4 \times C_{v(device)} \qquad (8)$$

The specific capacitance contributed by MnO_2 alone was calculated by subtracting the charge of the bare LSG framework according to the equation $C_{s,MnO2} = (Q_{LSG/MnO2} - Q_{LSG})/(\Delta V \times m_{MnO2})$ [31]. Here Q is the voltammetric charge, ΔV is the operating potential window and m is the mass.

Asymmetric cells. In order to achieve optimal performance with asymmetric supercapacitors, there should be a charge balance between the positive and negative electrodes. The charge stored by each electrode depends on its volumetric capacitance ($C_{v(electrode)}$), volume of the electrode (V), and the potential window in which the material operates (ΔE).

$$q = C_{v(electrode)} \times V \times \Delta E \qquad (9)$$

To attain the charge balance, the following condition must be satisfied

$$q_+ = q_- \tag{10}$$

$$\frac{V_+}{V_-} = \frac{C_{v(electrode)-} \times \Delta E_-}{C_{v(electrode)+} \times \Delta E_+} \tag{11}$$

The charge balance was achieved by adjusting the thickness of the positive and negative electrodes.

Comparison with commercial energy storage systems. In order to put the LSG/MnO_2 hybrid supercapacitors and micro-supercapacitors into perspective, we tested the performance of a wide range of commercially available energy storage systems for comparison. This includes activated carbon supercapacitors, a pseudo-capacitor (2.6 V, 35 mF), a battery-supercapacitor hybrid (lithium ion capacitor) (2.3 V, 220 F), an aluminum electrolytic capacitor (3 V, 300 µF) and a lithium thin-film battery (4 V/ 500 µAh). Activated carbon supercapacitors of varying sizes were tested: small size (2.7 V, 0.05 F), medium size (2.7 V, 10 F) and large size (2.7 V, 350 F). The activated carbon large cell (2.7 V, 350 F) was tested at a lower current density of 160 mA/cm^3 due to a limitation in our measuring equipment that provides 10 A maximum current. All the devices were characterized under the same dynamic conditions as the LSG/MnO_2 hybrid supercapacitors and micro-supercapacitors. Data for the Li battery are reproduced from ref. [22].

XPS analysis. XPS was successfully used for better understanding of the chemical composition and the oxidation state of Mn in the LSG/MnO_2 electrodes. The Mn 2p and Mn 3s spectra are presented in Fig. 3 F-G. The peaks of Mn $2p_{3/2}$ and Mn $2p_{1/2}$ are located at 642.1 and 653.9 eV, respectively, with a spin energy separation of 11.6 eV, which is in good agreement with data for Mn 2p states previously reported [18-24 in the main manuscript]. Toupin *et al.* showed that the peak separation of the Mn 3s doublet is related to the oxidation state of Mn in manganese oxides, where reference samples of MnO, Mn_3O_4, Mn_2O_3 and MnO_2 showed a separation of 5.79, 5.50, 5.41 and 4.78 eV,

respectively [32]. The as-prepared LSG/MnO_2 showed a separation energy of 4.8 eV for the Mn 3s doublet (Fig. 3G), suggesting that the oxide is MnO_2 which was further confirmed from the O 1s spectrum.

References

[1] Maiti S, Pramanik A & Mahanty S. Interconnected Network of MnO_2 Nanowires with a "Cocoonlike" Morphology: Redox Couple-Mediated Performance Enhancement in Symmetric Aqueous Supercapacitor. *ACS Appl. Mater. Interfaces* 6, 10754−10762 (2014).

[2] Huang M, Zhang Y, Li F, Zhang L, Ruoff RS, Wen Z & Liu Q. Self-Assembly of Mesoporous Nanotubes Assembled from Interwoven Ultrathin Birnessite-type MnO_2 Nanosheets for Asymmetric Supercapacitors. *Scientific Reports* 4, 3878 (2014).

[3] Zhi M, Xiang C, Li J, Li M, Wu N. Nanostructured carbon–metal oxide composite electrodes for supercapacitors: a review. *Energy Environ. Sci,* 5, 72-78 (2013).

[4] http://www.elton-cap.com/, retried on October 15, 2014.

[5] http://www.maxwell.com/products/ultracapacitors/125v-tran-modules

[6] Glavin ME, Chan PKW, Armstrong S & Hurley WG (2014) A stand-alone photovoltaic supercapacitor battery hybrid energy storage system. *Proc. Power Electron. Motion Control Conf.*, EPE-PEMC, 1688–1695.

[7] Simon P, Gogotsi Y (2008) Materials for electrochemical capacitors. *Nature Materials* **7**: 845-854.

[8] Chmiola J, Largeot C, Taberna PL, Simon P, Gogotsi Y (2010) Monolithic Carbide-Derived Carbon Films for Micro-Supercapacitors. *Science* 328:480-483.

[9] El-Kady MF, et al. (2012) Laser Scribing of High-Performance and Flexible Graphene-Based Electrochemical Capacitors. *Science* **335**:1326-1330.

[10] Zhu Y, Murali S, Stoller MD, Ganesh KJ, Cai W, Ferreira PJ, Pirkle A, Wallace RM, Cychosz KA, Thommes M., Su D, Stach EA, Ruoff RS (2011) Carbon-Based Supercapacitors Produced by Activation of Graphene. *Science* 332:1537-1541.

[11] Yang X, Cheng C, Wang Y, Qiu L, Li D (2013) Liquid-Mediated Dense Integration of Graphene Materials for Compact Capacitive Energy Storage. *Science* 341:534-537.

[12] Li P, et al. (2014) Core-Double-Shell, Carbon Nanotube@Polypyrrole@MnO_2 Sponge as Freestanding, Compressible Supercapacitor Electrode. *ACS Appl. Mater. Interfaces* **6**:5228−5234.

[13] Cheng Y, Lu S, Zhang H, Varanasi CV, Liu J (2012) Synergistic Effects from Graphene and Carbon Nanotubes Enable Flexible and Robust Electrodes for High-Performance Supercapacitors. *Nano Letters* 12: 4206-4211.

[14] Lee SW, Kim J, Chen S, Hammond PT, Shao-Horn Y (2010) Carbon Nanotube/Manganese Oxide Ultrathin Film Electrodes for Electrochemical Capacitors. *ACS Nano* 4:3889-3896.

[15] Patel MN, Wang X, Wilson B, Ferrer DA, Dai S, Stevenson KJ, Johnston KP (2010) Hybrid MnO_2–disordered mesoporous carbon nanocomposites: synthesis and characterization as electrochemical pseudocapacitor electrodes. *J. Mater. Chem.* 20:390–398.

[16] Fischer AE, Pettigrew KA, Rolison DR, Stroud RM, Long JW (2007) Incorporation of Homogeneous, Nanoscale MnO_2 within Ultraporous Carbon Structures via Self-Limiting Electroless Deposition: Implications for Electrochemical Capacitors. *Nano Lett.* 7:281–286.

[17] Wu ZS, Wang DW, Ren W, Zhao J, Zhou G, Li, Cheng, HM (2010) Anchoring hydrous RuO2 on graphene sheets for high-performance electrochemical capacitors. *Advanced Functional Materials* 20:3595-3602.

[18] Mazloumi M, Shadmehr S, Rangom Y, Nazar LF, Tang X. (2013) Fabrication of Three-Dimensional Carbon Nanotube and Metal Oxide Hybrid Mesoporous Architectures. *ACS Nano* 5:4281-4288.

[19] Ghidiu M, Lukatskaya MR, Zhao MQ, Gogotsi Y, Barsoum MW (2014) Conductive two-dimensional titanium carbide 'clay' with high volumetric capacitance. *Nature* 516:78-82.

[20] Ling Z, Ren CE, Zhao MQ, Yang J, Giammarco JM, Qiu J, Barsoum MW, Gogotsi Y. (2014) Flexible and conductive MXene films and nanocomposites with high capacitance. PNAS 111:16676-16681.

[21] Stoller MD, Ruoff RS (2010) Best practice methods for determining an electrode material's performance for ultracapacitors. *Energy & Environmental Science* 3:1294-1301.

[22] Pech D, et al. (2010) Ultrahigh-power micrometre-sized supercapacitors based on onion-like carbon. *Nature Nanotechnology* **5**:651-654.

[23] El-Kady MF & Kaner RB (2013) Scalable fabrication of high-power graphene micro-supercapacitors for flexible and on-chip energy storage. *Nature Communications* **4**:1475.

[24] Lin J, Zhang C, Yan Z, Zhu Y, Peng Z, Hauge RH, Natelson D & Tour JM (2013) 3-Dimensional Graphene Carbon Nanotube Carpet-Based Microsupercapacitors with High Electrochemical Performance. *Nano Lett.* 13: 72–78.

[25] Beidaghi M & Wang C (2012) Micro-Supercapacitors Based on Interdigital Electrodes of Reduced Graphene Oxide and Carbon Nanotube Composites with Ultrahigh Power Handling Performance. *Adv. Funct. Mater.* 22:4501-4510.

[26] Wang K, Zou W, Quan B, Yu A, Wu H, Jiang P & Wei Z (2011) An All-Solid-State Flexible Micro-supercapacitor on a Chip. *Adv. Energy Mater.* 1:1068–1072.

[27] Shen C, Wang X, Li S, Wang J, Zhang W, Kang F (2013) A high-energy-density micro supercapacitor of asymmetric MnO_2–carbon configuration by using micro-fabrication technologies. *Journal of Power Sources* 234:302-309.

[28] Feng J, Sun X, Wu C, Peng L, Lin C, Hu S, Yang J & Xie Y (2011) Metallic Few-Layered VS2 Ultrathin Nanosheets: High Two-Dimensional Conductivity for In-Plane Supercapacitors. *J. Am. Chem. Soc.* 133:17832–17838.

[29] Cao L, Yang S, Gao W, Liu Z, Gong Y, Ma L, Shi G, Lei S, Zhang Y, Zhang S, Vajtai R & Ajayan PM (2013) Direct Laser-Patterned Micro-Supercapacitors from Paintable MoS_2 Films. *Small* 9:2905–2910.

[30] Li D, et al. (2008) Processable aqueous dispersions of graphene nanosheets. *Nature Nanotechnology* 3:101-105.

[31] Lang X, et al. (2011) Nanoporous metal/oxide hybrid electrodes for electrochemical supercapacitors. *Nature Nanotechnology* **11**:232-236.

[32] Toupin M, et al. (2004) Charge storage mechanism of MnO2 electrode used in aqueous electrochemical capacitor. Chem. Mater. 16:3184-3190.